Chapter 2

Light source and experimental techniques

The use of a third-generation synchrotron radiation (SR) light source, a high-resolution monochromator, and advanced time-of-flight (TOF) techniques allows to measure high-resolution vacuum ultra-violet (VUV) spectra. A modern SR light source in combination with a undulator provides high photon flux from the infrared to hard x-rays region. The harmonic radiation from an undulator is selected by a monochromator and results in highly monochromatic light with high intensity, which is needed for the present photoionization measurements of doubly excited helium. The well-defined time structure of SR allows TOF electron spectrometers to measure photoelectron time spectra if the storage ring is operated in a single-bunch mode. This technique is particularly well suited for the present studies of channel- and angle-resolved measurements of doubly excited helium because of its high-resolution and good transmission particularly for slow electrons. In this chapter, I shall briefly introduce the properties of SR and monochromators as well as the TOF techniques. In addition, I shall briefly describe the gas cell, which was used for total ion yield measurements of doubly excited helium.

2.1 Properties of synchrotron radiation

A electron that undergoes an acceleration generates electromagnetic radiation (see Fig. 2.1(a)). If the photons are created by electrons with highly relativistic velocities in a circular orbit, this radiation is called SR (see Fig. 2.1(b)). The main difference to Fig. 2.1(a), which displays the non-directed emission pattern of an accelerated charged particle at non-relativistic velocities, is the strong forward direction of SR (Fig. 2.1(b)). Due to the relativistic velocity of the circulating electrons, the emission pattern of the radiation is dramatically pushed into forward direction (see Fig. 2.1). The opening half-angle Θ of the cone is proportional to $1/E$ and given by [47]

$$\Theta = \frac{1}{\gamma} = \frac{m_0 c^2}{E}, \tag{2.1}$$

where E is the electron energy, m_0 the rest mass of the electron, and c the velocity of light.

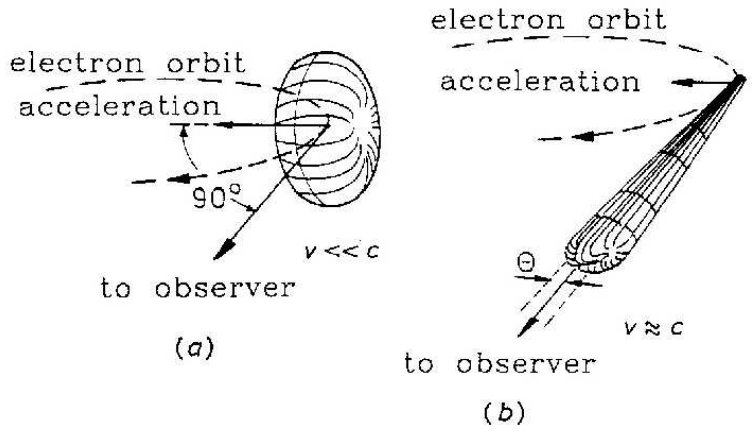

Figure 2.1: Emission pattern of an electron circulating with velocity v: (a) $v/c \ll 1$; (b) $v/c \approx 1$ (from Ref. [47, 48]).

In SR facilities that concentrate on the production of such radiation, the accelerated electrons are stored in a circular ring, called *electron storage ring*. An electron storage ring is composed of many technical components like injection system, microwave cavity for acceleration, bending magnets, focus magnets, vacuum system, and wiggler/undulator. The electrons are generated in an injection system consisting of an electron source and an accelerator, either a synchrotron or a linear acceleration. When the electrons are accelerated to the operating energy of the storage ring, they are injected into the storage ring. The bending magnets are used to deflect the electron beam which ensures the electrons to travel in a circular path. The bending magnets can also serve as the source of SR. In the straight section of the storage ring, a number of focus magnets such as quadrupole magnets are placed for the aim of focusing the electrons. The quadrupole magnets act much like glass lenses in light optics. In order to compensate the energy loss of the electrons during the SR emission, the electrons are accelerated each time as they pass through the RF cavity installed inside the electron storage ring. At the Berliner Elektronenspeicherring für Synchrotronstrahlung (BESSY II), a 500 MHz cavity is operated and results in a time period of 2 ns between two adjacent bunches. Taking 240 m circumference of the storage ring into account, a maximum number of 400 electron bunches can be injected in the multi-bunch operation mode, which was used for our total ion yield measurements presented in chapter 4. In the single-bunch operation mode at BESSY II, only one bunch is filled resulting in a pulse period of 800 ns, which defines the time window for the photoemission measurements with the TOF techniques.

In a simple picture, the wiggler or the undulator can be considered to consist of a large number of bending magnets (see Fig. 2.2), which results in high intensity radiation. When the electrons in the storage ring fly through a bending magnet, a wiggler or an undulator SR is generated. Physically, the undulator and wiggler have similar magnetic structures and they are typically a couple of meters long (more than 10-meter long undulators are operated in free-electron lasers (FEL)). In contrast to the smooth spectral distribution

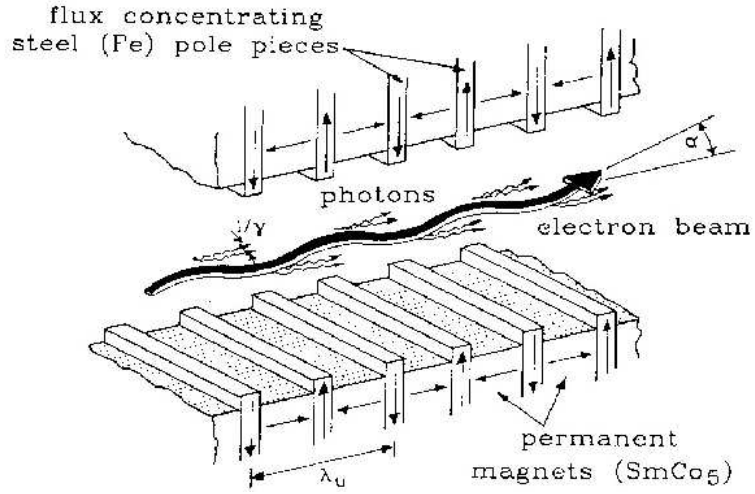

Figure 2.2: The transverse undulator with permanent magnets and iron poles providing a magnetic field with period λ_u. The maximum deflection angle α of the electron beam and the photon emission angle $\Theta = 1/\gamma$ at the maximum bending of the undulators are shown (From [47, 49]).

of radiation from a bending magnet or a wiggler, the radiation from an undulator shows characteristic maxima, which results from the periodic magnetic structure of the insertion devices illustrated in Fig. 2.2. Since it is composed of many bending magnets, the total photon flux radiated from a wiggler increases by a factor equal to the number of poles n in comparison to the radiation from a single bending magnet. In contrast to the radiation distribution of the wiggler, the undulator can produce quasi monochromatic radiation with high brightness peaks (see Fig. 2.3), where the peak intensity is higher by a factor of n^2 as compared to a single bending magnet.

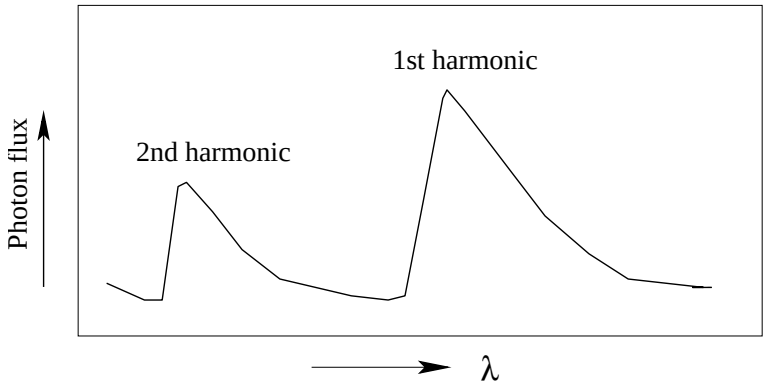

Figure 2.3: Photon flux distribution of an undulator for the first two harmonics.

The interference between electromagnetic waves emitted by the same electron at the different bending magnets of an undulator yields a redistribution of the spatial and spectral intensity. For the radiation emitted at angles Δ and Λ with respect to the

undulator axis, one gets [47]

$$\lambda_n = \frac{\lambda_u \Theta^2}{2n}\left[1 + \frac{K^2}{2} + \frac{\Delta^2 + \Lambda^2}{\Theta^2}\right], \tag{2.2}$$

where λ_n is the wavelength of the nth harmonic radiation ($n = 1$ is the fundamental radiation); λ_u is the magnetic period; Δ and Λ refer to the angles of the radiation emitted in the plane parallel to and perpendicular to the permanent magnets, respectively. $K = \gamma\alpha \propto B_0\lambda_u$ is a characteristic parameter for these devices. Here α and B_0 are the maximum deflection angle and the strength of magnetic field on the axis of the electron beam. Due to the weak magnetic field B_0 and the small period λ_u of the magnetic structure, which cause a small deviation angle α, the undulator has smaller values of K than the wiggler. The essential difference between a wiggler and an undulator lies in the magnetic field strength B_0.

The harmonics are the characteristics of an undulator spectrum as shown in Fig. 2.3, where the first and the second harmonic are plotted. In order to collimate the undulator light, a small size aperture is placed behind the undulator. Since harmonics with even number are off axis, only odd ones are selected to go through the aperture. According to the energy region required for an experiment, one can choose the harmonic, which provides high photon flux. For doubly excited helium, photon energies from 65 to 79 eV are required so that the 1st harmonics was applied due to its high photon flux. During the measurement, the gap between the permanent magnets of the insertion device has to be adjusted in order to maintain a high photon flux over the whole photon-energy range of the measurement.

2.2 Properties of monochromator

The harmonic radiation of an undulator has to be monochromatized and focused on the spot, where the experiment is performed, via a beamline containing some collimating and focusing elements such as grating, slits, and mirrors.

The present measurements of the PCSs and the ADPs of doubly excited helium were performed at beamline U125/2-SGM (BUS) of BESSY II, which employs a spherical grating monochromator (SGM). The optical layout of the BUS beamline is schematically displayed in Fig. 2.4. The two prefocusing and refocusing mirrors M_1 and M_3, respectively, are placed in the front and at the end of beamline. An exit slit S_2, placed in front of M_3, can be adjusted depending on resolution and flux. For the present measurements, high resolution is needed, and a small aperture of the exit slit S_2 was therefore used. In order to enhance the quality of focused light, an entrance slit S_1 is normally placed behind the prefocusing mirror M_1 in the SGM beamline. The monochromator is a key part and is located in the center of the beamline; it selects a narrow band of the photon energies from the broad energy range of SR and, in addition, focuses the monochromatic light on the exit slit.

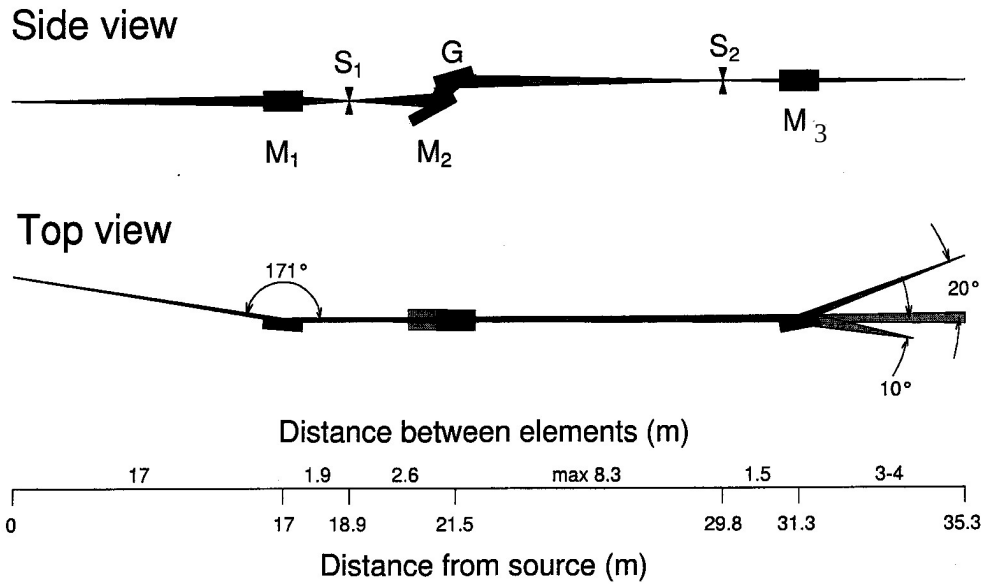

Figure 2.4: Optical layout of spherical grating monochromator in beamline U125/2-SGM at BESSY II (from Ref. [50]).

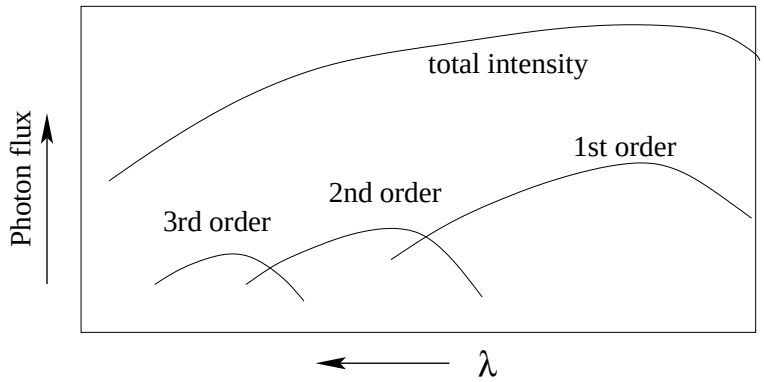

Figure 2.5: Photon flux distributions from a monochromator with the first three orders. The total intensity contains the monochromatized light of all orders.

For a spherical or plane grating of the monochromator, the diffraction from its surface obeys the same equation,

$$m\lambda = d \cdot (\sin\zeta + \sin\eta), \tag{2.3}$$

where d is the distance between successive grooves, m the diffraction order, λ the diffracted wavelength, ζ and η the angles of incidence and diffraction, respectively. ζ and η can be varied by a rotation of the grating, which results in a change of the diffracted wavelength, i.e. the photon energy is selected by varying the angles of incidence and diffraction, ζ and η. Except for the selection of light, the spherical grating has the additional function to focus the diffracted light onto the exit slit. When the wavelength of light is varied, the distance of the focus to the exit slit varies. This is the reason why an

additional plane mirror (M_2 in Fig. 2.4) is installed in the monochromator, which can match the focus requirement by an adjustments of ζ and η as well as of the distance between grating and light source without having to move the position of the exit slit. In order to avoid a loss of flux, large angles of incidence ζ are applied in gracing-incidence monochromators for high photon energies. In contrast to gracing-incidence monochromators, a normal incidence monochromator with smaller angles ζ is used measurements ($E_{photon} \leq 30$ eV) for low photon energies.

The proper choice of the numbers of grooves of a grating is mainly determined by the energy region of interest. A spherical grating with a groove density of 1100 l/mm is used for the present PCS and ADP measurements of doubly excited helium for photon energies from 65 to 79 eV.

In Fig. 2.5, the photon flux distributions as a function of wavelength is given for different diffraction orders. The first, second, and third orders of monochromatized light are represented by $m = 1$, 2, and 3 in Eq. (2.3), respectively. According to experimental needs to the flux and the resolution of interest, one can choose the first order of light to gain the flux or the second order of light for higher resolution.

2.3 Gas ionization cell

The measurements of the total photoionization cross section were performed with an ionization cell shown schematically in Fig. 2.6; it contains a two-plate ionization chamber with an active length of 10 cm. The ionization cell was pumped to a pressure of $\leq 10^{-8}$ mbar and then filled with $5 - 1000$ μbar of the gas under study (noble gas, N_2, CO, O_2, etc.); for helium, the pressure was $\cong 0.5 - 1$ $m$bar. One electrode, used as a repelled electrode, is kept at about +100 V; at the other electrode, the photoionization current in the $10^{-15} - 10^{-12}$ A range is recorded as a function of photon energy by a commercial pico-Ampere-meter (Keithley 6517). The ionization chamber is separated from the ultrahigh vacuum (UHV) of the monochromator (in the 10^{-10}-mbar range) by a 1500-Å-thick Aluminum or 1000-Å-thick Carbon window. In order to avoid disturbing effects due to absorption edges of the window (e.g., Al 2p (at $\cong$ 73 eV) or C 1s ($\cong$ 284 eV)), the window material was selected according to the photon-energy range studied. For photon energies from 65 to 79 eV in care of doubly excited helium, a carbon window was accordingly used for total-ion-yield measurements. Because the windows cannot withstand pressure differences exceeding $\cong 10$ $m$bar, special attention was taken during the pump-down of the ionization chamber.

The gas cell was also used for determining the photon energy resolution. The achievable energy resolution, ΔE, depending on the incident photon energy, E, the diffraction order, m, the finite size of the exit slit, ΔE_s, the finite size and stability of the beam source, ΔE_b, as well as the finite quality of the optical elements, ΔE_e, can be expressed by [21],

$$\Delta E \propto E^{3/2} m^{-1/2} (\Delta E_s^2 + \Delta E_e^2 + \Delta E_b^2)^{1/2}. \tag{2.4}$$

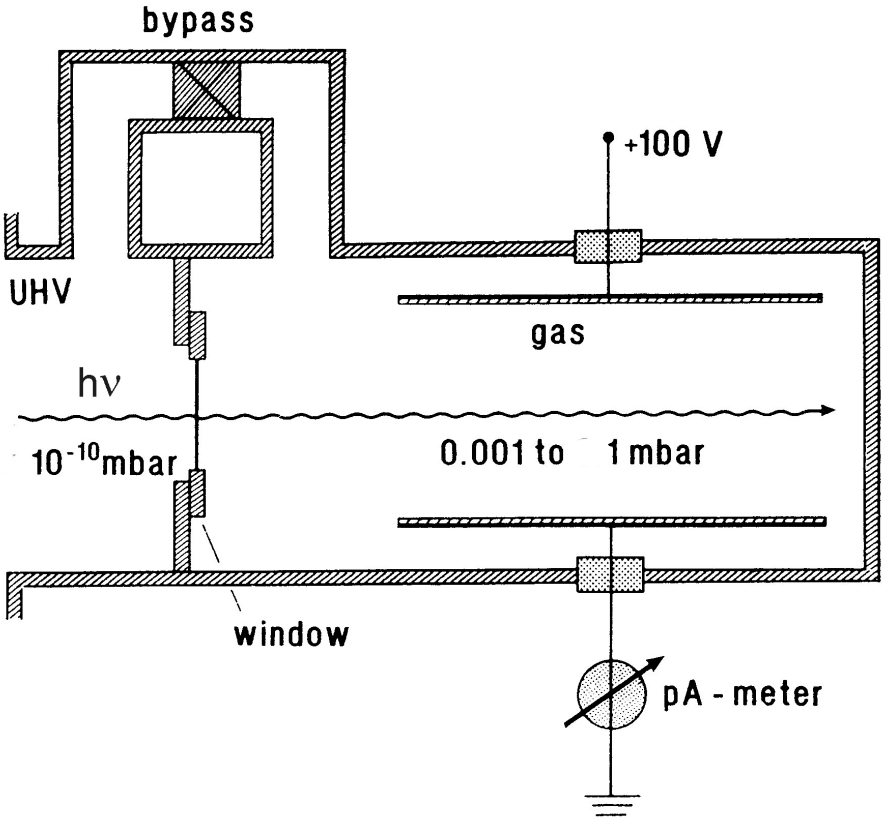

Figure 2.6: Schematic view of the ionization cell (from [21]).

In order to achieve high photon flux, the first order, $m = 1$, was chosen in our measurements, as mentioned before. ΔE_s depends linearly on the width s of the exit slit. The actual adjustment of the exit slit is a competition between count rate and energy resolution. For the total-ion-yield measurements (the TOF measurements), a photon energy resolution (FWHM) of $\cong 1.7$ meV ($\cong 6$ meV) were used. Normally, the resonance $2, -1_3$ is employed for a characterization of photon resolution. It therefore serves as a bench mark for the optimization of mirror positions, the size and position of the exit slit, etc.

2.4 Time-of-flight techniques

About 40 years ago, the pulsed nature of SR emitted from electron storage rings provided the basis for the development of time-of-flight (TOF) electron spectroscopy as an efficient, but relatively low-resolution alternative to electrostatic or magnetostatic analyzers. Early TOF electron spectrometers were used for photoemission experiments on solid samples where a lower absolute energy resolution could be tolerated [51]. Since the 80's of the last century, detectors and timing electronics for TOF electron spectrometers for gas-phase experiments were developed [22, 52]. In the present dissertation, the photoelectron time spectra for studies of the PCSs and the ADPs in doubly excited helium were taken by TOF electron spectrometers, which allow to determine the kinetic energies

of various outgoing electrons. Consequently one can determine the principal quantum numbers n of the remaining electron in $He^+(n)$ and in this way n-specific PCSs and ADPs are achieved.

In the TOF technique, the kinetic energies of the photoelectrons are determined by measuring the flight times of the electrons from the interaction region to the detector, which are typically of the order of some tens to hundred nanoseconds. This method inherently relies on a timing pulse directly correlated to the SR light pulse, and a signal provided by the electron detector. The time spectra of electrons with various kinetic energies can be collected simultaneously. In oder to avoid an overlap of slow photoelectrons originating from one pulse and fast photoelectrons coming from the next pulse, the time window, i.e. the pulse period, has to be long enough to ensure the arrival of the electrons with the lowest velocity. Therefore, the single-bunch mode of SR is used to match such a time window.

One advantage of a TOF spectrometer in comparison to an electrostatic analyzer is that it can collect the entire electron spectrum simultaneously. Due to this, the background noise in the time spectrum is suppressed since it is evenly distributed over the entire time spectrum; this fact greatly increases the signal-to-noise ratio for the weak structures analyzed in this work. Another advantage of the TOF technique is that, due to its simplicity and small size, more than one spectrometer can be mounted to an experimental chamber. This allows to perform angle-resolved measurements without rotating the chamber so that the available beamline can be used more efficiently. In the "ball-chamber" used for the measurements of the ADPs (see Figs. 5.2 and 5.3), more than 10 TOFs can be mounted in the dipole plane. In addition, TOF spectrometers have a high transmission for photoelectrons with low kinetic energy down to ≅50 meV.

2.4.1 Time-of-flight electron spectrometer

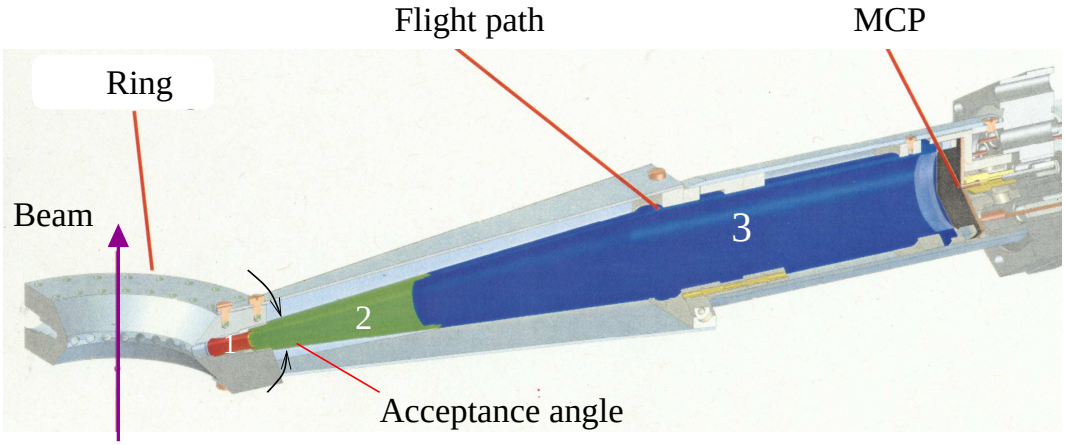

Figure 2.7: Schematic for the design of TOF electron spectrometer. The drift tube for electron flight path contains three parts marked by 1, 2, and 3, respectively. (From M. Braune)

The TOF spectrometer employed for the measurements of the ADPs is schematically

shown in Fig. 2.7; it is similar to the TOF spectrometer used in the PCS measurements. Three accelerating potentials, normally less than 2 eV, can be applied to parts 1, 2, and 3 in the drift tube that has a length of 28.1 cm. The TOF spectrometers are spatially fixed by a ring perpendicular to the beam indicated by the vertical arrow in Fig. 2.7; the acceptance angle of the TOF spectrometer is $5° - 6°$. To detect the electrons, a multi-channel plate (MCP) was installed at the end of the drift tube. For this particular TOF spectrometer design, the total flight distance of photoelectrons from the interaction region to the MCP is about 30.9 cm.

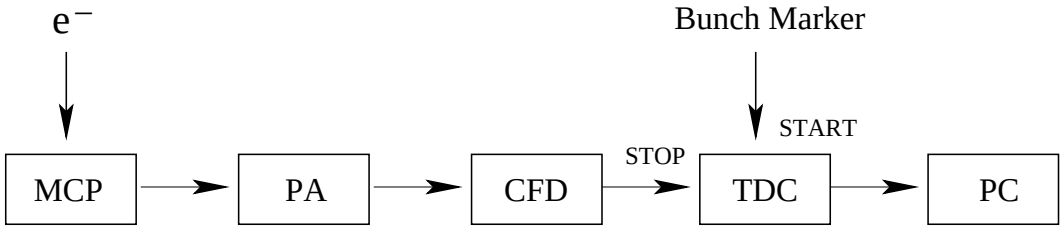

Figure 2.8: Schematic of the data-acquisition electronics.

Fig. 2.8 shows schematically the electronics used for processing the MCP pulses from one TOF analyzer. The electrons are detected by three MCPs, with diameter of $\cong$ 34 mm diameter, in a Z-stack arrangement. Normally, an operating voltage of 3000 V is applied to the MCP that has a resistance of $50 - 100$ MΩ. The signals are first amplified using a preamplifier (PA) and then reach a constant-fraction discriminator (CFD), where signal noise is suppressed by setting an reasonable threshold as a trigger point. The CFD output signal is a fast timing pulse that is used for the "stop" signal for the time-to-digital-converter (TDC). The "start" signal is provided by the bunch marker that is correlated to the SR pulse. The time difference between "start" and "stop" is converted in the TDC into channel numbers, which are recorded and stored by a computer. In the single-bunch mode of BESSY II, the time window between two adjacent pulses is 800 ns. This time period represents 13385 channels, each channel having a time resolution of $\cong$ 60 ps.

2.4.2 Time-to-Energy conversion

In this dissertation, the TOF photoelectron time spectra were taken at different photon energies using a step-width of 3 meV, and they have to be first converted into photoelectron energy spectra by a time-to-energy conversion in order to obtain differential cross sections (DCS). Time spectra taken directly from a TOF electron spectrometer are not linear in energy (see Eq. (2.5)) resulting in an asymmetric shape, especially for peaks with low kinetic energies; this can be seen in Fig. 2.9. Therefore, it is necessary to linearize the spectrum in energy without affecting the peak area (proportional to the number of counts). The relationship between the flight time t and the kinetic energy

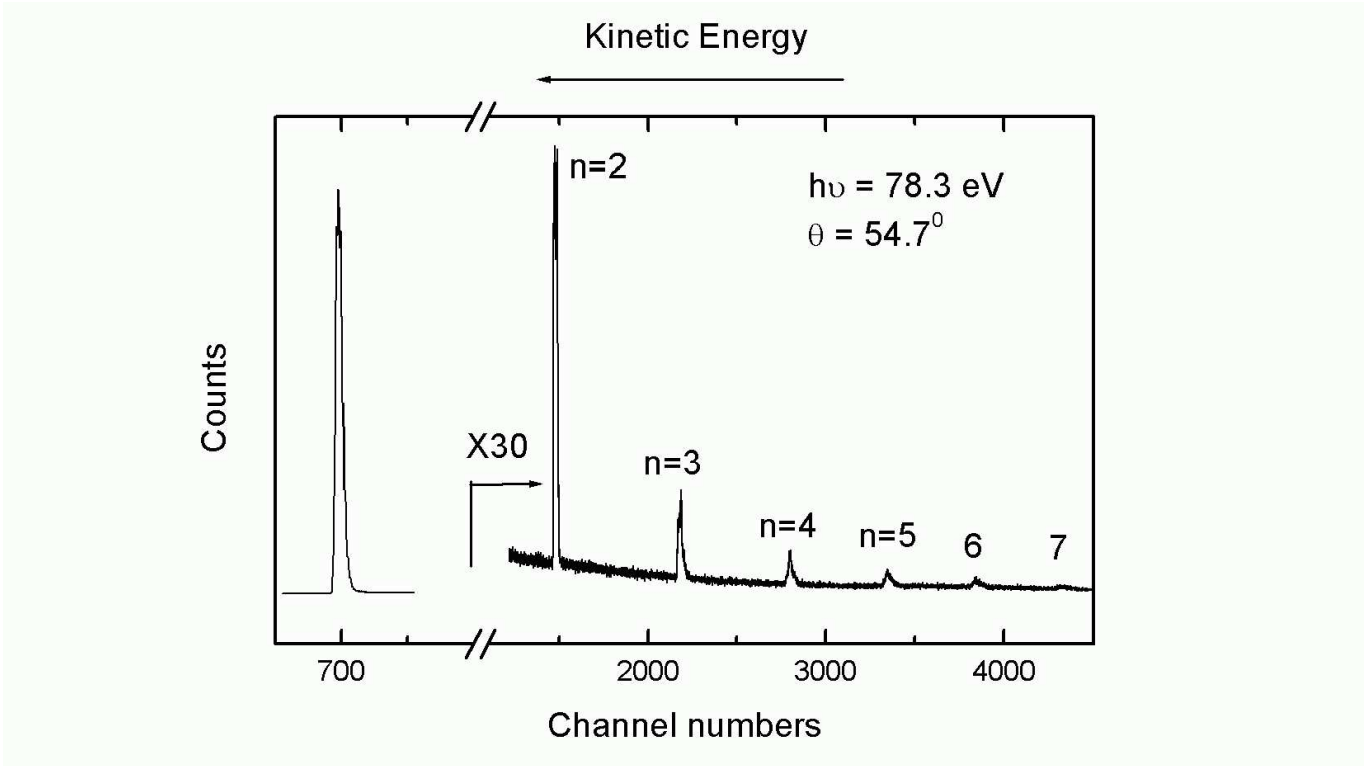

Figure 2.9: Photoelectron spectrum on the time scale taken at a photon energy of 78.3 eV. n indicate the decay channels that lead to a final state $He^+(n)$. The channel numbers are proportional to the flight time of the photoelectron in contrast to the kinetic energy, which is increasing in the opposite direction.

E_{kin} of an electron under field-free conditions is given by

$$E_{kin} = \frac{1}{2} m_e v^2 = \frac{m_e l^2}{2t^2}, \tag{2.5}$$

with m_e being the electron mass and l the distance from the interaction region to the detector. In oder to improve the transmission, in particular for slow electrons, the spectra were measured with an accelerating voltage (E_{pot}), and thus Eq. (2.5) cannot be applied without precise knowledge of all the electrical potentials in the analyzer. An empirical expression has to be used for the relation between kinetic energy and the corresponding channel. Considering this correspondence between a channel in the time spectrum (ch) and the flight time (t) ($t \propto (prompt\text{-}ch)$), one can rewrite Eq. (2.5) as

$$E_{kin}(ch) - E_{pot} \propto \frac{1}{(prompt - ch)^2}. \tag{2.6}$$

Here the prompt describes a peak in the time spectrum that originates from photons scattered from the gas target. Due to the high velocity of light, the flight time from the interaction center to the detector can be neglected and the corresponding peak can be used as zero on the time axis. One can fit this formula to some peaks with known kinetic energies in the time spectra. With the fit result, one can transform a time spectrum into an energy spectrum by a point-to-point transformation. A precise time-to-energy

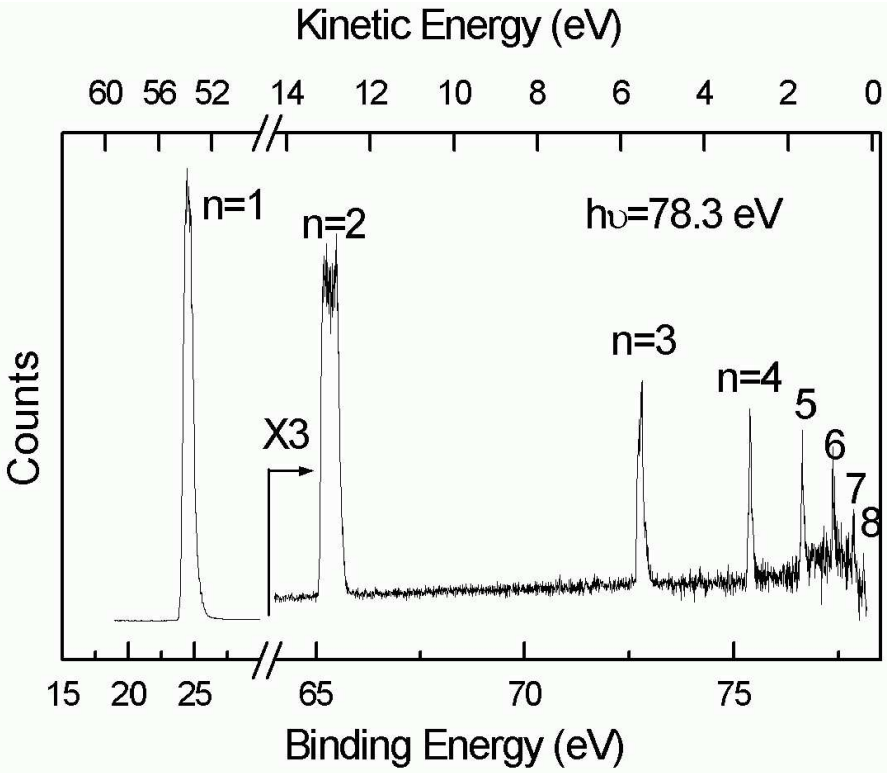

Figure 2.10: Photoelectron spectrum on the energy scale taken at a photon energy of 78.3 eV and obtained from the spectrum on the time scale in Fig. 2.9 by time-to-energy conversion. The corresponding kinetic energies are marked on the upper x-axis.

conversion is difficult to obtain for low-energy electrons because the paths of the electrons are strongly influenced by residual magnetic fields. As a result, the kinetic-energy axis cannot be determined accurately by a simple fit based on Eq. (2.6). It is necessary to use a polynomial fit function to obtain a complete and accurate time-to-energy conversion. In this dissertation, the electrons with kinetic energies down to 0.3 eV were taken in the measurements of the PCSs and the ADPs. Only high-quality fit curves can guarantee the conservation of the spectra in the time-to-energy conversion procedure, in particular for low-count peaks with low kinetic energies. The high accurate time-to-energy conversion can convert the peaks, corresponding to one of final ion states $He^+(n)$ with various photon energies, to an exactly the same binding energy scale. Then, the DCSs are obtained automatically by the Sunny program [53] by evaluation of the counts in an energy window on the binding energy axis containing these peaks. Otherwise, the peaks in the energy spectra (as a function of binding energy) can experience a shift with respect to different photon energies, which causes the loss of counts during the extraction of the DCSs.

As an example, the spectrum taken at a photon energy of 78.3 eV at $\theta = 54.7°$ was converted from the time scale given in Fig. 2.9 to the energy scale presented in Fig. 2.10. After conversion, the peaks become symmetric and their widths as well as relative intensities vary in the spectrum on the energy scale.

The kinetic-energy resolution, $\Delta E/E$, of an electron TOF spectrum is given by [54]

$$\frac{\Delta E}{E} = \sqrt{\left(\frac{2\Delta t}{t}\right)^2 + \left(\frac{2\Delta l}{l}\right)^2 + \left(\frac{2\Delta \lambda}{\lambda}\right)^2}; \tag{2.7}$$

it depends on the relative uncertainties in the wavelength ($2\Delta\lambda/\lambda$), the flight time ($2\Delta t/t$), and the electron flight-path length ($2\Delta l/l$). The latter is determined by the size of the interaction region, typically 100-1000 μm, the analyzer acceptance angle (5°), and the variation in the length of flight path. Due to the small acceptance angle, the total variation of the electron flight length should be less than 3 mm. In summary, the kinetic-energy resolution is estimated to be about 2% of the kinetic energy. For a detailed discussion of electronics, see Ref. [54].

2.4.3 Transmission function and analyzer efficiency

The slow electrons are lost more easily during the drift process towards the detector. This can result from residual magnetic or electric fields inside the chamber. In oder to effectively detect very slow electrons, accelerating voltages are applied to the drift tube. However, even for this case, the counts for slow electrons may decrease dramatically, in particular for electrons with kinetic energies below 1 eV. Therefore, a transmission correction has to be applied in order to convert the counts for slow electrons into partial relative cross section.

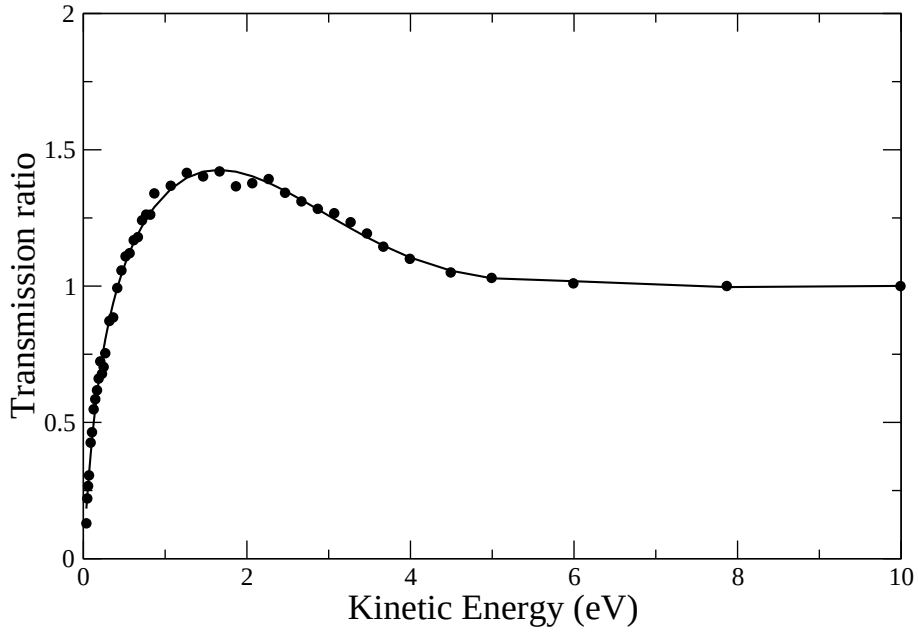

Figure 2.11: Transmission function as a function of photoelectron kinetic energy. Solid points are our experimental data for the satellite $n = 2$ of helium; the solid line is the fit to the function given in Eq. (2.8).

Fig. 2.11 displays a typical transmission correction function for a TOF electron spectrometer derived from the fit to our experimental cross section for the satellite $n = 2$ of

helium. Experimental data are shown as solid points below the kinetic energy of 10 eV. Here, the transmission correction function employed for the fit has the form

$$y = p_1 \cdot exp(-x/p_2) + p_3 \cdot x + p_4 \cdot x^2 + p_5 \cdot x^3, \tag{2.8}$$

where p_1 to p_5 are free fit parameters. y and x represent the transmission correction factor and the kinetic energy, respectively. After determining the parameters in Eq. (2.8) by a fit, this function can be employed to correct the cross sections for any satellite with the same kinetic energy. Above kinetic energies of 10 eV, no transmission correction is performed, i.e. the transmission correction factor for photoelectrons with high kinetic energies is assumed to be unity.

For a measurement of the β parameter, besides transmission correction, the TOF efficiency has to taken into account. Due to differences in TOF spectrometer design, the potential of MCP, and the electronics, TOF efficiencies could vary within a factor of 2. For helium spectra, the efficiency factors for various TOFs can be extracted from a comparison of the $1s$ lines. This is due to the following facts: first, the kinetic energy of photoelectron from the $1s$ line is quite high ($E_{kin} > 50$ eV in the present region concerned) and, consequently, these fast electrons are not affected by the transmission or underlying magnetic fields; second, the efficiency of a TOF spectrometer is assumed to be independent of the kinetic energy of the photoelectrons. In addition, the angular distribution parameter $\beta_{1s} = 2$ has to be taken into account. For 90^0 TOF in the absence of $1s$ peak, one can determine its efficiency factor by a photoelectron line having a $\beta \neq 2$ such as Ne^+ 2p emission line [55].